An Automatic Site Survey Approach for Indoor Localization using a Smartphone

Qing Liang[1], *Student Member, IEEE* and Ming Liu[1], *Senior Member, IEEE*

***Abstract*—Opportunistic signals (e.g., WiFi, magnetic fields, ambient light, etc.) have been extensively studied for low-cost indoor localization, especially via fingerprinting. We present an automatic site survey approach to build signal maps in space-constrained environments (e.g., modern office buildings). The survey can be completed by a single smartphone user during normal walking, say with little human intervention. Our approach follows the classical GraphSLAM framework: the front-end constructs a pose graph by incorporating the relative motion constraints from pedestrian dead-reckoning (PDR), the loop-closure constraints by magnetic sequence matching with the WiFi signal similarity validation, and the global heading constraints from the opportunistic magnetic heading measurements; and the back-end generates a globally consistent trajectory via graph optimization to provide ground truth locations for the collected signal fingerprints along the survey path. We then build the signal map (a.k.a, fingerprint database) upon these location-labeled fingerprints by Gaussian processes regression (GPR) for later online localization. Specifically, we exploit the pseudo wall constraints from the GPR variance map of magnetic fields, and the observations of ceiling lights to correct the PDR drifts with a particle filter. We evaluate our approach on several datasets collected from both the HKUST academic building and a shopping mall. We demonstrate real-time localization on a smartphone in an office area, with 50th percentile accuracy of 2.30 m and 90th percentile accuracy of 3.41 m.**

***Note to Practitioners*—This paper was motivated by the problem of efficient signal map construction for fingerprinting-based localization on smartphones. The conventional manual site survey method, known to be time-consuming and labor-intensive, hinders the penetration of fingerprinting methods in practice. This paper suggests a GraphSLAM-based approach to automate this signal map construction process by reducing the survey overhead significantly. A surveyor is merely asked to walk through an indoor venue with an Android smartphone held in hand with little human intervention. Meanwhile, opportunistic signals (e.g., WiFi and magnetic fields) are captured by smartphone sensors. We construct a GraphSLAM engine to first identify the measurement constraints from these signal observations and then recover the surveyor's walking trajectory by graph optimization. We can generate signal maps using the captured signals alongside the recovered trajectory. In this paper, we propose a WiFi signal similarity validation method to reduce false positive loop-closures and exploit magnetic headings to improve trajectory optimization performance. In addition, we propose to use the generated magnetic field variance map and the lights distribution map for localization. The efficacy of the proposed site survey approach is proved through field experiments and real-time localization is demonstrated on a smartphone using the generated signal maps. The localization experiment was conducted by a single user with the same Android smartphone that was used in the site survey. Therefore, the usability of signal maps on other devices and the generality to other users, have not yet been testified. We will leave these issues in our future work.**

***Index Terms*—Indoor localization, GraphSLAM, site survey, opportunistic signals.**

*This work was supported by National Natural Science Foundation of China No. U1713211, the Shenzhen Science, Technology and Innovation Commission (SZSTI) JCYJ20160428154842603 and JCYJ20160401100022706, the Research Grant Council of Hong Kong SAR Government, China, under Project No. 11210017 and No. 21202816, all awarded to Prof. Ming Liu.

[1]Qing Liang and Ming Liu are with the Department of Electronic and Computer Engineering, Hong Kong University of Science and Technology. qing.liang@connect.ust.hk, eelium@ust.hk

I. Introduction

INDOOR localization using smartphones has drawn much attention in recent years due to the ever-rising demand for accurate location awareness of location-based services (LBSs) indoors [1]. Many solutions [2]–[6] have been introduced by exploring the rich sensory modalities and powerful computational resources commonly available on modern mobile devices. By leveraging ultrasonic or visible light communication, the state-of-the-art localization technologies [2], [3] can deliver high location accuracy (say in centimeters) using commodity smartphones, yet at the cost of necessary additional infrastructure (e.g., ultrasonic beacons [2] and modulated LED lights [3], [7]). Meanwhile, opportunistic signals (e.g., WiFi signal strength and geomagnetic fields) have been extensively studied for low-cost localization, where the meter-level accuracy is attainable via fingerprinting [4]–[6], [8], [9]. Free of any investment on the infrastructure or hardware modification, fingerprinting approaches using opportunistic signals are more cost-effective ways to penetrate some indoor LBS applications, such as pedestrian navigation in a large building.

The general framework of fingerprinting-based localization entails two phases: offline fingerprint database (a.k.a, signal map) construction that associates the collected signal fingerprints with physical locations, and online location determination by comparing the newly observed fingerprint against the pre-built signal map. Significantly, an accurate and up-to-date signal map is critical to the good location performance of fingerprinting approaches. The conventional approach to signal map construction–*manual site survey*–requires some trained experts to explore the whole area of interest comprehensively and collect fingerprints at a regular grid of survey points with known locations that are usually obtained with a physical floor plan. In particular, a periodic update of the map, normally by site re-survey, is required to maintain the long-term localization performance as fingerprints are vulnerable to environmental dynamics (e.g., furniture rearrangement). As a result, the manual site survey is time-consuming and labor-intensive for both the signal map creation and maintenance, especially in practical deployment at scale.

Many research efforts have been devoted to alleviating this deficiency. Among the existing proposals, *path survey* proves to be effective in reducing time and effort, and has been successfully adopted by many research works, such as [4], [10]–[12], and some commercial indoor location services (e.g., Google Indoor Maps[1] and IndoorAtlas[2]). The core of path survey is to collect signal fingerprints continuously along a walking trajectory, instead of separately at a set of discrete points. In particular, the trustworthy trajectory with certain accuracy provides "ground truth" locations for the collected fingerprints. The signal map would be trivial to build upon these location-labeled fingerprints, e.g., by means of regression tools like Gaussian processes regression (GPR) [13].

However, it remains challenging to obtain the walking trajectory accurately and efficiently. Some approaches [4], [10] resort to a physical floor plan by planning a set of waypoints at strategic locations (e.g., corners) for the surveyors to follow, and the intermediate locations in between are derived via time interpolation or dead reckoning. Still, they entail some human intervention, e.g., determining some waypoints and walking along. Meanwhile, crowdsourcing-based solutions [14]–[19] try to distribute the survey task to numerous normal users who are willing to share their local sensing data from the common environment. Yet, the data quality is not guaranteed due to the unconstrained user behaviors and heterogeneous devices. Additionally, crowdsourcing techniques suffer from slow convergence to a usable signal map in the bootstrapping stage due to their data-hungry nature [4]. Moreover, many established crowdsourcing solutions require the physical floor plans as a prior [14]–[16], yet, such knowledge may not be readily accessible to the public due to privacy concerns.

Further, Simultaneous Localization and Mapping (SLAM) technologies [11], [12], [20]–[22] were employed to help automate the site survey process in unknown buildings. These solutions show great effectiveness in recovering the survey trajectory to build the signal map without detailed knowledge of the building. SLAM algorithms for robots benefit from reliable ego-motion estimation using wheel encoder odometry, and accurate environment modeling with high-quality sensors (e.g., Lidar and RGB-D camera) [23]–[25]. By contrast, the odometry information for smartphone users is less reliable, normally obtained via pedestrian dead-reckoning (PDR) by step-counting [26]. Moreover, the poor sensing capabilities of the low-cost smartphone sensors (e.g., WiFi scanners) render it more difficult to capture the geometry properties of the environment and to build an accurate observation model.

Recently, magnetic sequence matching has been successfully exploited to identify loop-closure constraints to solve the SLAM problem [11], [12], [27]. The geomagnetic signals are often disturbed by local magnetic anomalies from building construction materials and electronic equipment [28]. The spatial-varying and temporal-stable nature make magnetic signals good location signatures [4]. The major challenge for magnetic matching based loop-closure detection arises from the increasing false positives in large-scale environments [12] due to the poor global uniqueness of magnetic signatures. To reduce false loop-closures, Gao et al. [27] impose a strong assumption on the spatial distance between each pair of matching sequences by limiting the search space of each sequence to its spatial vicinity. This assumption may be problematic in large-scale environments due to the severe PDR drift over time. To relax this assumption, Wang et al. [12] propose to combine both the magnetic sequence and the PDR-derived motion patterns into a keyframe for more reliable loop-closure detection. The rationale is to reduce mismatches by checking the local trajectory topology. Its efficacy tends to degrade in certain scenarios with less motion diversity, e.g., a rectilinear office building. Another concern for magnetic matching is that its success relies on both rich magnetic anomalies in the surroundings and highly consistent walking trajectories each time the user revisits a place, particularly due to the limited coherence distance of magnetic signals [27]. To this end, the existing systems [12], [27] usually assume a space-constrained environment, e.g., an office building.

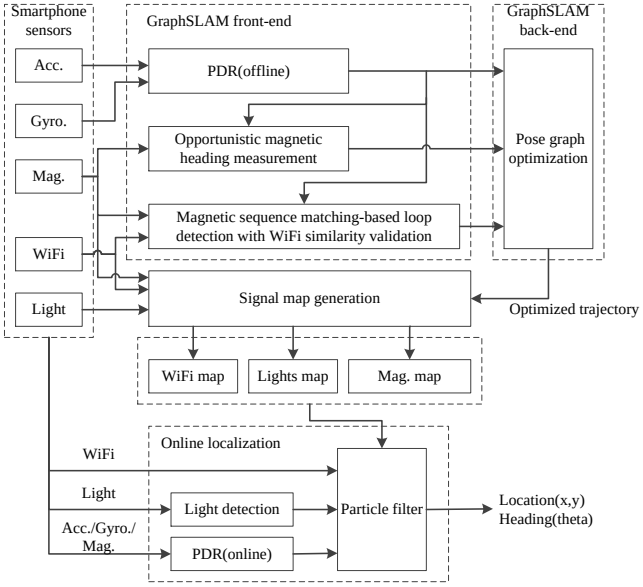

Fig. 1: Overview of the proposed site survey approach.

In this paper, we propose an automatic site survey approach for low-cost indoor localization using opportunistic signals via fingerprinting, particularly in unknown buildings and with little human intervention. Fig. 1 illustrates the overall system architecture. We advocate the use of path survey, and, more specifically, the SLAM-based survey path recovery to automate the signal map construction. Inspired by [12] and [27], our approach follows the generic offline GraphSLAM framework [29], including a front-end that populates an initial pose graph with constraints, and a back-end that optimizes the graph to be most consistent with these constraints. The walking trajectory can be thus recovered by graph optimization. In particular, we also adopt the magnetic sequence matching method to identify loop-closure constraints, and use PDR to provide motion constraints for the front-end creation. To make the magnetic matching scheme tractable, we assume a space-constrained environment with rich magnetic distortions,

[1]https://www.google.com/maps/about/partners/indoormaps/
[2]http://www.indooratlas.com/

e.g., a modern office building of rectilinear shape. We use the recovered trajectory poses as ground truth to associate opportunistic signals with physical locations during the site survey. Therefore, we can generate signal maps for later online localization, e.g., by Bayesian filtering. Nevertheless, our approach differs in several respects, and we will detail them in the following.

Note that too many false positive loop-closures could severely deteriorate the graph optimization in the back-end. To reduce false positives in magnetic matching, we first divide the whole magnetic sequence into multiple segments at strategic locations with salient motion patterns (e.g., turns), and search loop-closures among a limited number of magnetic sequence segments, which are checked to ensure they are long enough and feature rich signal variances. By contrast, Gao et al. [27] compared the magnetic sequences within a fix-sized sliding window. Our approach can limit the search space of magnetic matching, and more valuably, reduce mismatches by choosing the informative magnetic sequences. Yet, false positives remain. Orthogonal to the previous works, we exploit the similarity of WiFi signal sequences for loop-closure validation. This idea is inspired by the complementary nature of the magnetic signals and WiFi signals: the former has high spatial resolution but poor global uniqueness, whereas the latter has good global uniqueness but low spatial resolution.

Despite the pervasive existence of magnetic fields, we claim that both the magnetic anomalies and undistorted geomagnetic fields are indeed opportunistic. As is well known, indoor magnetic anomalies normally arise from ferromagnetic materials (e.g., steel-reinforced concrete) in building structures. The anomaly distribution is thus heavily site-dependent. We observe in some places (e.g., far away from magnetic sources) that magnetic signals are dominated by geomagnetic fields, i.e., with little distortion by surroundings. Such "clean" magnetic signals may not be informative enough for loop-closure detection, but meanwhile, provide us an opportunity to obtain noiseless magnetic headings for GraphSLAM optimization. Inspired by this observation, we introduce the opportunistic magnetic heading measurements to the GraphSLAM front-end by carefully identifying magnetic distortions and removing error-prone heading measurements. The resulting benefits are two-fold: 1) global heading information is available for the optimized trajectory, and 2) map consistency is improved with measurements in addition to the loop-closure constraints.

To briefly conclude, the front-end builds on the PDR-derived motion constraints, the magnetic matching-based loop-closure constraints after the WiFi signal similarity validation, and the global heading constraints from the opportunistic magnetic heading measurements. The walking trajectory can be recovered by graph optimization in the back-end. We use GPR to generate the fine-grained signal maps for both the WiFi and magnetic signals. Note that the WiFi maps can provide the global location information, and thus enable the *push-to-fix* localization. Localization follows the standard Bayesian filtering framework where PDR provides the motion model, and opportunistic signal measurements provide the observation model using the generated signal maps. Different from the authors in [27], who declared the uselessness of magnetic maps in localization, we observe that the GPR variance map of the magnetic fields resembles well the building layout. We propose to use the generated magnetic variance map as a pseudo floor plan to correct the PDR drift with a particle filter. Additionally, we exploit the observations of ceiling lights that are distributed linearly along narrow corridors to further constrain the PDR drift. We evaluate the proposed automatic site survey approach on six real-world datasets, collected both from the office buildings on the HKUST campus and public areas outside. We demonstrate the feasibility of the generated signal maps for real-world localization and deliver reasonable accuracy using a smartphone in real time.

Our contributions are summarized as follows:

1) We propose a loop-closure validation method based on the similarity of WiFi signal sequences, to reduce false positives in the loop-closure detection using magnetic sequence matching;
2) We introduce the opportunistic magnetic headings to the GraphSLAM front-end, for the first time to our knowledge, with improved optimization results;
3) We exploit the GPR variance map of magnetic fields as a pseudo floor plan and the ceiling lights along the corridor to correct the PDR drift for online localization with a particle filter.

The remainder of this paper is organized as follows. Section II introduces the related work. In Section III, we detail the GraphSLAM-based site survey incorporating the loop-closure validation method based on the WiFi signal similarity and the opportunistic magnetic heading measurements. Section IV introduces particle filtering-based online localization using the generated signal maps. In Section V, we present the evaluation results and discussions. Section VI concludes this paper.

II. Related Work

A. Pedestrian Dead-reckoning

PDR tracks relative user movements with inertial sensors, typically an inertial measurement unit (IMU) on the smartphone, carried by the walking individuals. The dominating PDR systems follow the step-and-heading principle, generally incorporating step detection, step length estimation and heading change estimation [26]. They offer good short-term tracking performance using inexpensive IMUs without any infrastructure support by exploiting some domain-specific knowledge of human walking patterns. Step events are triggered by monitoring the repetitive cycles in inertial sensor readings, e.g., using peak detection. The step is characterized by a step vector $\mathbf{s}_i = (\ell_i, \delta\theta_i)$, where ℓ_i is the estimated step length, and $\delta\theta_i$ the heading change at time index i. The raw PDR trajectory can be obtained by accumulating these consecutive step vectors. However, PDR suffers from significant drift over time [26]. The incorrect step detection and inaccurate step length estimation render it less reliable compared to the wheel encoder odometry used by mobile robots. To counter these issues, extrinsic information, such as structural constraints from building floor plans, is needed. In particular, the wall-constrained particle filter has been adopted by many researchers [4], [14] to constrain the PDR drift.

B. Opportunistic Signals for Localization via Fingerprinting

In this context, the ambient signals that can be used for localization purposes are referred to as opportunistic signals. They can either naturally exist (e.g., geomagnetic fields) or come from the existing infrastructure intended for other usages (e.g., WiFi). WiFi signals continue to be exhaustively studied for localization, particularly via fingerprinting [5], [20]. Magnetic signals indoors are often accompanied by local magnetic anomalies from building materials and electronic equipment in operation. The spatial-varying and temporal-stable nature of magnetic signals make them good location features [4], [10], [28]. In addition, unmodulated lighting fixtures (e.g., fluorescent lights) have also been exploited for localization [6], [30]. Modern buildings are enriched with WiFi signals, magnetic fields, and visible light from lighting fixtures. As they are readily perceivable by smartphone sensors, we envision all of them as valuable opportunistic signals for localization.

C. Signal Map Construction by Crowdsourcing

As mentioned previously, a manual site survey is costly for signal map creation. Many crowdsourcing-based solutions are proposed to alleviate this situation [14]–[18]. The basic idea is to crowdsource the survey task to a lot of users carrying mobile devices. Path survey techniques have been adopted by most crowdsourcing solutions. The major difference lies in the method of obtaining the walking trajectories of normal users. Zee [14] used a wall-constrained particle filter to estimate the user's trajectory by fusing the relative motion with the building floor plan, and then the location-labeled WiFi signal fingerprints were used for signal map generation. UnLoc [15] identified a set of landmarks, namely the seed landmarks at strategic locations on a floor plan and the organic landmarks with distinct signal signatures, to correct the PDR drifts. However, the availability of physical floor plans may be problematic for some buildings due to security concerns. Some research works [31], [32] can reconstruct the sketch of the floor plan (e.g., pathways) using crowdsourcing techniques, and accordingly build the signal maps. The potential challenge for these works arises from the slow convergence to a usable map in the bootstrapping phase.

D. GraphSLAM with Opportunistic Sensing

GraphSLAM-based methods [12], [20], [21], [27] can build signal maps during a user's normal walking by using PDR and opportunistic sensing, even without floor plans. Huang et al. [20] first formulated the WiFi signal strength SLAM as a GraphSLAM problem. They came up with a WiFi measurement model under the assumption that the signal strength measurements are interpretable at nearby locations. This assumption requires dense WiFi sampling in the testing area to ensure reasonable interpretability, yet at the cost of longer survey time and human-labor. In fact, due to the slow WiFi scanning rate, [20] took a 17-min-long walk in a relatively small area ($60\,\mathrm{m} \times 10\mathrm{m}$) to collect 536 WiFi samples. Gao et al. [27] and Wang et al. [12] proposed to use magnetic sequence matching-based loop-closure detection and PDR-derived motion measurements within a GraphSLAM framework. Yet only a few efforts were made to reject false loop-closures. In this work, we propose to exploit the signal similarity of WiFi sequences to further reduce the false positives in loop-closure detection.

III. GraphSLAM-based Automatic Site Survey

In this section, we introduce the GraphSLAM-based offline site survey, including 1) a GraphSLAM front-end composed of PDR, opportunistic magnetic heading measurements, and magnetic sequence matching-based loop-closure detection with WiFi signal similarity validation; 2) a GraphSLAM back-end for pose graph optimization; and 3) signal map generation.

A. PDR

We adopt a simple PDR algorithm based on zero-crossing detection using the inbuilt inertial sensors on a smartphone. To avoid the side effects of magnetic distortions, we only use the accelerometer and gyroscope for attitude and heading estimation. We perform step detection by monitoring the gait cycling pattern exhibited in vertical accelerations. To further estimate the step length, we exploit an empirical step length model [33], assuming the correlation between the step length and the largest difference in vertical accelerations. Its formulation is $\ell = k\sqrt[4]{a_z^{max} - a_z^{min}}$, where a_z^{max} and a_z^{min} are the maximum and minimum vertical accelerations during each step, and k is a constant parameter. To obtain the correct metric scale of PDR poses, we need to do an offline calibration of the model parameter, i.e., by collecting accelerometer readings together with ground truth walking profiles.

B. Loop-closure Detection using Magnetic Sequence Matching with WiFi Signal Similarity Validation

We detect turns on the raw PDR trajectory, and then split the whole magnetic sequence collected during walking into multiple segments at these turns. Loop-closures are identified by magnetic sequence matching and then validated by the WiFi signal similarity checking to reduce false positives.

1) Turn detection: As mentioned above, we assume a space-constrained indoor environment with narrow corridors interconnected at salient turns (e.g., left/right/U-turn). The narrow corridors impose strong geometry constraints on the user's movements and secure the consistency of walking trajectories each time the user revisits a place. The highly consistent trajectories are critical to the successful magnetic matching due to the limited coherence distance of magnetic signals. As turn-taking is a salient motion pattern, we can easily exploit the detected turns to segment the whole magnetic sequence into sub-sequences for later loop detection.

Turns generate salient variations (e.g., peaks and valleys) of the curvature on the PDR-derived trajectory. We perform turn detection by computing the local curvature of the trajectory within a sliding window. We find all the peaks and valleys, as turn candidates, in the sequence of curvatures with sufficient magnitude. Thereafter, we split the whole trajectory into multiple segments. Note that false positives may occur

because of the user action. For instance, the trajectory may be bent temporally due to a user's side movement during door opening. Under such circumstances, we will merge these consecutive segments if they are checked to be in a line. To this end, we compare the accumulated walking distance within the sliding window, and the chord distance joining the start and end points of the two consecutive segments. If the difference is fairly small, we may safely conclude that they are in a line and should be merged together. The magnetic signal sequence will be sliced into multiple segments as per the detected turns. To reduce mismatches, only those informative segments are selected, with sufficient traveling distances and significant signal variations.

2) Loop-closure detection using magnetic matching: The magnetic signals collected by walking users suffer from the spatial sampling density variation problem [4] due to both varying walking speeds and different sensor sampling rates. To counter this problem, we use dynamic time warping (DTW) [4] to match these magnetic sequences. DTW proves to be effective in measuring the similarities between time-varying signal series. As the user may revisit the same place in the opposite direction, we compare every magnetic sequence pair in both directions. With the alignment between two magnetic sequences, the step-wise loop-closure constraints between the walking trajectories can be easily determined by timestamps.

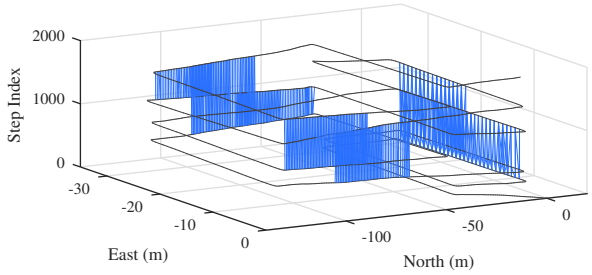

(a) True positive loop-closures shown on the optimized trajectory stretched along z-axis for better visualization

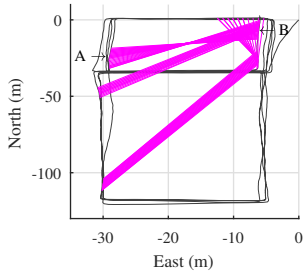

(b) False positives shown on the optimized trajectory

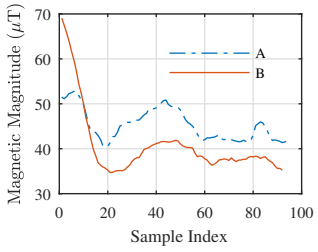

(c) Magnetic sequences at location A and B, marked on (b)

Fig. 2: Illustration of loop-closure detection by magnetic matching.

Fig. 2a illustrates the correct loop-closures detected by magnetic matching. The pair-wise loop-closures are shown as blue lines connecting distinct poses on the optimized trajectory from one of the collected datasets. These loop-closures exhibit considerable spatial consistency between the overlapped walking trajectories. False positives may occur (see Fig. 2b), as magnetic sequence matching is error-prone due to the inevitable magnetic ambiguities (see Fig. 2c), especially in large-scale environments. For instance, loop-closures between trajectory segments A and B are incorrect, as they are indeed on two opposite corridors. The corresponding magnetic sequences, as shown in Fig. 2c, are very similar to each other in shape, despite the fairly long samples in use. We will address this problem in the next section.

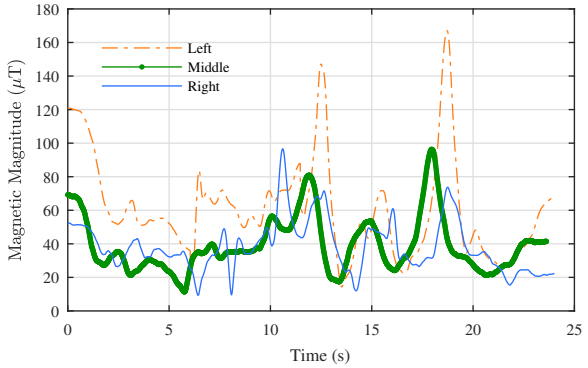

Fig. 3: Effect of survey path consistency on magnetic matching.

Note that we assume a space-constrained environment with rich magnetic anomalies for our approach to work properly. The success of magnetic sequence matching heavily relies on spatially consistent survey paths characterized by differentiable magnetic sequence profiles. In specific, the spatial diversity of a magnetic sequence improves with its sequence length and the occurrences of neighboring magnetic anomalies. Additionally, the spatial consistency of two overlapping paths (say with potential loop-closures) is critical to the successful matching of the two sampled magnetic sequences, due to the small coherence distance (around 30 cm [27]) of magnetic signals. Even small deviations of the walking paths can probably cause severe signal distortions of the magnetic sequence profiles, making DTW fail to match them by checking the shape. To demonstrate this effect, we have collected magnetic sequences using a smartphone by walking along a 1 meter-wide corridor for three times. Each time we follow a route with slightly different lateral offsets, i.e., the left side, the middle and the right side. The magnitudes of the three sequences are shown in Fig. 3. We can clearly observe that they are quite different in shape from one another. Remind that DTW tries to match two signal sequences exactly by comparing their shape. Therefore, inconsistent walking paths can make two magnetic sequences fail to match. Walking trajectories are more likely to be consistent in a space-constrained environment since the surveyor's freedom of movement is tightly limited by the geometry layout (e.g., narrow corridors). By contrast, the spatial consistency in an open area tends to be worse due to the lack of geometry constraints.

3) Loop-closure validation using WiFi signal similarity: The adopted loop-closure detection method suffers from an increasing number of false positives in large-scale environments due to the inherent ambiguities of magnetic signals. To alleviate this situation, we need a loop-closure validation mechanism to help reduce false positives. As we know, magnetic fields with anomalies are inherently local features with a good spatial resolution, yet lacking global uniqueness. By taking advan-

tage of the spatial diversity of magnetic anomalies, we can improve their distinctiveness by using a group of sequential magnetic measurements (a.k.a., magnetic sequence profiles). However, global uniqueness cannot be guaranteed. As shown in Fig. 2c, it happens that two magnetic sequences drawn at faraway locations may have similar profiles. Therefore, DTW-based magnetic matching could be easily confused by such ambiguities and result in false positives.

By contrast, WiFi fingerprints[3] are global features which are less differentiable in local regions. The WiFi fingerprints are characterized by unique MAC addresses and can be globally referenced. Especially, their global uniqueness will improve with the deployment density of WiFi access points (APs). The similarity of any two fingerprints generally decreases with their spatial separation due to the radio signal propagation loss, especially in scenarios with complex building layouts. For example, we can tell that two WiFi fingerprints should be different at faraway locations and be similar when nearby. Meanwhile, it remains difficult to differentiate those fingerprints within a confined neighborhood. Inspired by the complementary nature of WiFi and magnetic signals, we exploit the observed WiFi signals to help detect false loop-closures due to the mismatching of magnetic sequences, by examining the WiFi signal similarity properties. Specifically, we assume a reasonably dense deployment of WiFi APs in modern buildings.

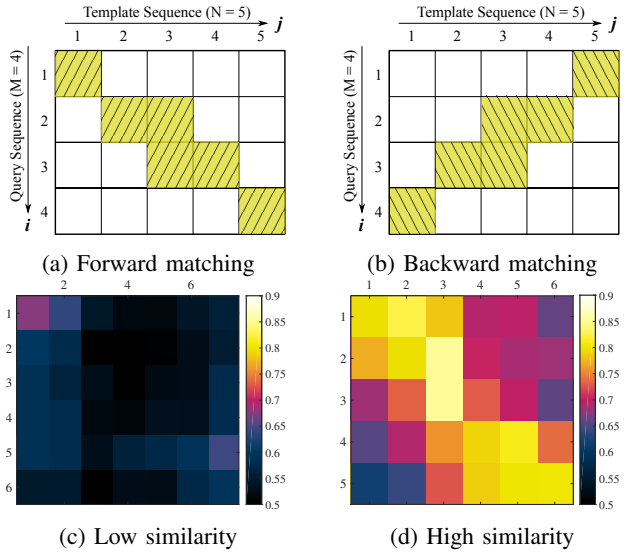

Fig. 4: (a) and (b) show the similarity measurement metric between two timestamped WiFi sequences. (c) and (d) show the example of similarity matrices in our field test.

To account for the low spatial resolution issue of WiFi signals, we use a sequence of sequential fingerprints to improve their distinctiveness. That is, we group WiFi fingerprints collected along the walking trajectory into a sequence of timestamped measurements. To compare the similarity between

[3]The WiFi fingerprint at any given location is composed of RSSI measurements of all the heard APs in each scan session. That is, we treat the WiFi fingerprint as a vector, while the RSSI measurement for each separated AP as a scalar. Additionally, we assume that the RSSI measurements for different APs are independent by following the convention in related literature.

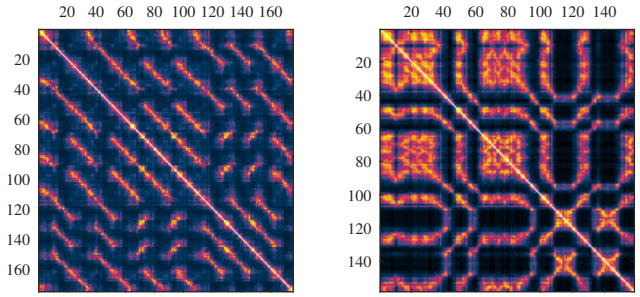

Fig. 5: Similarity matrices of WiFi fingerprints in typical indoor settings: an office building (a) and a shopping mall (b).

two given WiFi sequences, we propose a sequence-wise WiFi signal similarity metric, as shown in Fig. 4. In the illustration example, we have $\mathrm{M} = 4$ samples in the query sequence and $\mathrm{N} = 5$ samples in the template sequence. We first create a similarity matrix for the two given candidate sequences, i.e., by computing the similarity values for each pair of fingerprint samples. Specifically, we utilize a normalized squared exponential kernel function to measure the similarity between each two vectorized fingerprints, ranging from 0 (i.e., poorest case) to 1 (i.e., best case). As reported by the loop detection module, the surveyor may close a loop (say revisiting parts of original routes) either in the same or opposite moving direction. Since all signals evolve with time, the candidate WiFi sequences, as well as corresponding magnetic sequences, are probable to match in either chronological order (a.k.a., forward matching) or reverse chronological order (a.k.a., backward matching). In the case of forward matching, we take the average similarity of all the diagonal entries as a measure of the sequence-wise similarity. Otherwise, as shown in Fig. 4b, the back-diagonal entries will be used. Fig. 4c shows an example of the similarity matrix for two WiFi sequences collected at different locations (marked on Fig. 2b), where false loop-closures are reported by magnetic matching. We may clearly observe that the similarity values of all the entries are very low. These false positives can be trivially identified and then rejected. In another example, we show the similarity matrix for true positive loop-closures in Fig. 4d. We can observe high similarity values on its diagonal entries (e.g., corresponding to the forward matching case). Subject to insufficient spatial distinctiveness of WiFi signals, our method may fail in certain scenarios where false positive loop-closures are reported at nearby locations. Yet we find it can work quite well in practice, e.g., in terms of rejecting a majority of false positives.

Note that we exploit the spatial diversity of WiFi signals, which can be affected by the building's physical settings. Given the same AP deployment density, WiFi fingerprints are more distinctive in a space-constrained environment than in a large open area. For example, the concrete wall and pillar partitions in a modern office building can increase the spatial diversity of WiFi signals, e.g., due to the blockage and reflection of walls and other obstacles like doors. As a result, the effectiveness of loop-closure validation can be affected by the WiFi signal properties experienced in different survey

scenarios. To illustrate the effects, we build the similarity matrix using the complete WiFi fingerprints collected in each survey, as shown in Fig. 5. Fig. 5a shows the result in a typical office building with wall partitions and narrow straight corridors. Fig. 5b shows the result in a shopping mall lack of wall partitions and with wide passages.

C. Opportunistic Magnetic Heading Measurements

In this section, we consider another case where the clean geomagnetic fields dominate the surrounding magnetic signals. The typical magnetic coherence distance is around 30 cm [27], which reveals that the magnetic fields from given magnet sources vary fast across space. We observe that magnetic signals measured by the smartphone held by a walking user are fairly stable in some open spaces and wide corridors. This is because in such circumstances smartphone sensors are far away from the steel building materials, e.g., in the supporting pillars. On the one hand, magnetic signals with rich local anomalies are more spatially unique and informative, rendering them good candidates for loop detection. On the other hand, the undisturbed magnetic signals could provide global heading measurements relative to Earth. To our knowledge, these measurements have rarely been used in previous works in creating the GraphSLAM front-end.

Algorithm 1 Opportunistic magnetic heading measurements.

Input:
Raw readings: acc. $\{\mathbf{a}_{t_n}\}_{n=1}^{\mathrm{N}}$, gyro. $\{\mathbf{w}_{t_n}\}_{n=1}^{\mathrm{N}}$, and mag. $\{\mathbf{m}_{t_n}\}_{n=1}^{\mathrm{N}}$, number of sensor samples N;
PDR odometry: $\{(\delta\theta_{t_k}, \ell_{t_k})\}_{k=1}^{\mathrm{K}}$, number of steps K;
Output:
Opportunistic magnetic headings Θ at certain steps S;

compute orientations $\{\hat{\theta}_{t_n}^{\text{magn}}\}_{n=1}^{\mathrm{N}}$ relative to magnetic North using $\mathbf{a}_{t_n}$, $\mathbf{w}_{t_n}$, and $\mathbf{m}_{t_n}$;
for each $n \in [1, \mathrm{N}]$ **do**
  $sin\theta_n \leftarrow \sin \hat{\theta}_{t_n}^{\text{magn}}$, $cos\theta_n \leftarrow \cos \hat{\theta}_{t_n}^{\text{magn}}$;
end for
$\Theta \leftarrow \emptyset$, $S \leftarrow \emptyset$, $w = 7$
for each $k \in [1, \mathrm{K} - w + 1]$ **do**
  $\langle rot\_angle, arc\_len \rangle \leftarrow getCurvature(\{(\delta\theta_{t_i}, \ell_{t_i})\}_{i=k}^{k+w-1})$;
  $std\_sin\theta \leftarrow std\left(\{sin\theta_n\}_{t_k \le t_n \le t_{k+w-1}}\right)$;
  $std\_cos\theta \leftarrow std\left(\{cos\theta_n\}_{t_k \le t_n \le t_{k+w-1}}\right)$;
  $\bar{\theta} \leftarrow averageAngle\left(\{\hat{\theta}_{t_n}^{\text{magn}}\}_{t_k \le t_n \le t_{k+w-1}}\right)$;
  if rot_angle, arc_len, $std\_sin\theta$, and $std\_cos\theta$ meet certain threshold conditions; **then**
    $S \leftarrow S \cup \{k\}$, $\Theta \leftarrow \Theta \cup \{\bar{\theta}\}$;
  end if
end for
return S, Θ;

We opportunistically derive the magnetic headings when local magnetic distortions are neglectable. The proposed algorithm, as shown in Algorithm 1, is straight-forward but effective in practice. The intuition here is that if we keep walking along a straight corridor, the magnetic heading should be constant in addition to bounded variations caused by the human's walking pattern. This is the case when the geomagnetic fields dominate the instant magnetic signals. We may safely assume that the magnetic signals are undisturbed if the magnetic heading measurements are stable over a period of time during the straight line walking.

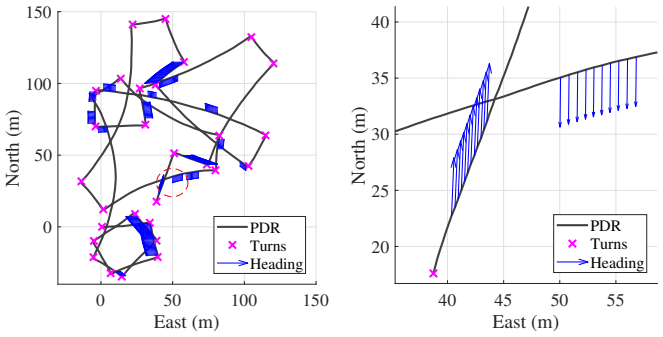

(a) Raw PDR path with turns and opportunistic magnetic headings

(b) Magnified view of headings in the dashed oval area of (a)

Fig. 6: Example results of PDR, turn detection and opportunistic magnetic heading measurements in a rectilinear office building.

First, we compute the magnetic headings using the raw magnetometer readings without considering the distortions. The derived magnetic headings are error-prone due to local anomalies. To reject errors, we exploit the PDR-derived motion patterns. To be specific, we iterate over the derived poses, and compute the curvature of the walking trajectory within a sliding window, along with the variations of magnetic headings. We assert a straight walking pattern if the curvature is small enough. Upon the identification of bounded heading variations, we consider that the magnetic heading is correct with reasonable uncertainties. In practice, we choose a sliding window size of 7 steps. To account for the angle singularity problem (i.e., transition from $-\pi$ to π and vice versa), we use the sin and cos values for variation calculation instead. The average angle value within the sliding window is adopted as the final magnetic heading measurement. We show an example in Fig. 6 with opportunistic magnetic headings and turns marked on a raw PDR trajectory.

D. Pose Graph Optimization

In this context, we define the pose graph as a collection of $SE(2)$ poses of the user's walking trajectory: $\mathbf{x} = \{\mathbf{x}_1^{\mathrm{T}}, \mathbf{x}_2^{\mathrm{T}}, \cdots, \mathbf{x}_{\mathrm{N}}^{\mathrm{T}}\}^{\mathrm{T}}$, where the ith pose is $\mathbf{x}_i = (x_i, y_i, \theta_i)^{\mathrm{T}}$, and N is the number of poses. The signal map is a model of the surrounding world expressed in the signal space with raw sensor measurements (e.g., WiFi signal strength and magnetic field strength) collected at historical user poses.

Given the kth measurement $\mathbf{z}_k$ and its prediction $\hat{\mathbf{z}}_k(\mathbf{x})$, we can compute the residue $\mathbf{e}_k(\mathbf{x})$ as follows:

$$\mathbf{e}_k(\mathbf{x}) = \mathbf{z}_k - \hat{\mathbf{z}}_k(\mathbf{x}),$$

where $\hat{\mathbf{z}}_k(\mathbf{x})$ is obtained via the observation model for the given measurement type. By assuming the independence

among these measurements, the total cost function can be formulated as

$$\mathrm{F}(\mathbf{x}) = \sum_k \mathbf{e}_k(\mathbf{x})^{\mathrm{T}} \mathbf{\Omega}_k \mathbf{e}_k(\mathbf{x}),$$

where $\mathbf{\Omega}_k$ is the information matrix for the kth measurement. The optimized poses $\mathbf{x}^*$ could be obtained by minimizing the cost function in quadratic form as

$$\mathbf{x}^* = \arg\min_{\mathbf{x}} \mathrm{F}(\mathbf{x}).$$

This can be solved by some non-linear least square solvers like the Gaussian-Newton method. Particularly, the PDR trajectory provides the initial guess for the optimization.

We introduce three types of measurement constraints to the initial pose graph, namely the odometry constraints from PDR, the loop-closure constraints from magnetic matching, and the global heading constraints from the opportunistic magnetic heading measurements. Accordingly, the cost function can be divided into three terms:

$$\mathrm{F}(\mathbf{x}) = \mathrm{F}_{\text{odom}}(\mathbf{x}) + \mathrm{F}_{\text{loop}}(\mathbf{x}) + \mathrm{F}_{\text{head}}(\mathbf{x}),$$

and they can be further expanded as follows:

$$\begin{aligned}
\mathrm{F}_{\text{odom}}(\mathbf{x}) &= \sum_{(i,j)\in\mathcal{P}} \mathbf{e}_{ij}^{\text{odom}}(\mathbf{x})^{\mathrm{T}} \mathbf{\Omega}_{ij}^{\text{odom}} \mathbf{e}_{ij}^{\text{odom}}(\mathbf{x}) \\
\mathrm{F}_{\text{loop}}(\mathbf{x}) &= \sum_{(i,j)\in\mathcal{Q}} \mathbf{e}_{ij}^{\text{loop}}(\mathbf{x})^{\mathrm{T}} \mathbf{\Omega}_{ij}^{\text{loop}} \mathbf{e}_{ij}^{\text{loop}}(\mathbf{x}) \\
\mathrm{F}_{\text{head}}(\mathbf{x}) &= \sum_{i\in\mathcal{R}} \mathbf{e}_{i}^{\text{head}}(\mathbf{x})^{\mathrm{T}} \mathbf{\Omega}_{i}^{\text{head}} \mathbf{e}_{i}^{\text{head}}(\mathbf{x}),
\end{aligned}$$

where $\mathcal{P}$ is the set of odometry constraints and $\mathcal{Q}$ is the set of loop-closure constraints between pose pairs; $\mathcal{R}$ is the set of global heading constraints for the given poses with opportunistic magnetic heading measurements; $\mathbf{\Omega}_{ij}^{\text{odom}}$, $\mathbf{\Omega}_{ij}^{\text{loop}}$ and $\mathbf{\Omega}_{i}^{\text{head}}$ are the respective information matrices. The residue term $\mathbf{e}_{ij}^{\text{odom}}(\mathbf{x})$ or $\mathbf{e}_{ij}^{\text{loop}}(\mathbf{x})$ is the relative transformation in $SE(2)$ between two poses i and j. $\mathbf{e}_{i}^{\text{head}}(\mathbf{x})$ can be computed as

$$\mathbf{e}_{i}^{\text{head}}(\mathbf{x}) = \theta_i^{\text{magn}} - \hat{\theta}_i,$$

where θ_i^{magn} is the global heading obtained by the opportunistic magnetic heading measurements, and $\hat{\theta}_i$ is the heading angle of the ith pose ($i \in \mathcal{R}$).

We use g2o [34] to implement the above-mentioned graph optimization. As false positive loop-closures may occur even after the WiFi signal similarity-based validation, we use the robust Huber kernel in g2o to alleviate this situation.

E. Signal Map Generation

Built upon the globally consistent walking trajectory from the GraphSLAM back-end, we can associate the collected opportunistic signals with "ground truth" locations in the survey environment, i.e., without the assumption of a physical floor plan. The location-labeled fingerprint samples are further used for signal map generation, e.g., by regression or classification. The signal map characterizes, either deterministically or probabilistically, the spatial evolution of certain signal properties across the surveyed space. For example, a deterministic representation is similar to a look-up table of signal measurements indexed by spatial locations. More often, we prefer a probabilistic model with additional knowledge of measurement uncertainties, in order to achieve localization by Bayesian filtering.

We hereafter consider three sources of scalar measurements with 2D location annotations, namely the WiFi RSSI for each AP, the magnetic magnitude, and the light intensity. We employ GPR to generate probabilistic maps for the WiFi signals and the magnetic field magnitudes. Next, we will detail the application of GPR in signal map generation following the convention in [13]. We consider a training dataset $\mathcal{D} = \{(\mathbf{x}_1, y_1), (\mathbf{x}_2, y_2), \ldots, (\mathbf{x}_n, y_n)\}$ sampled from a noisy process $y_i = f(\mathbf{x}_i) + \epsilon$, where ϵ is an additive Gaussian noise with zero mean and known variance σ_n^2. $\mathbf{x}_i \in \mathbb{R}^2$ is the 2D location and $y_i \in \mathbb{R}$ is the scalar observation at time instant t_i. For brevity, all $\mathbf{x}_i$ are aggregated into a design matrix $\mathbf{X} = [\mathbf{x}_1\, \mathbf{x}_2 \ldots \mathbf{x}_n]^{\mathrm{T}} \in \mathbb{R}^{n\times 2}$, and y_i into a column vector $\mathbf{y} = [y_1\, y_2 \ldots y_n]^{\mathrm{T}} \in \mathbb{R}^n$.

Gaussian processes (GPs) are exploited to predict the posterior distributions over functions f from the training set $\mathcal{D}$. The covariance between two function values $f(\mathbf{x}_p)$ and $f(\mathbf{x}_q)$ can be characterized by a kernel function $k(\mathbf{x}_p, \mathbf{x}_q)$. We normally choose the squared exponential (a.k.a., RBF) kernel,

$$k(\mathbf{x}_p, \mathbf{x}_q) = \sigma_f^2 \exp\left[-\frac{|\mathbf{x}_p - \mathbf{x}_q|^2}{2l^2}\right], \tag{1}$$

where the signal variance σ_f^2 and the length scale l specify together how strongly the two samples are correlated. The covariance for the noisy observations y_p and y_q is $\mathrm{cov}(y_p, y_q) = k(\mathbf{x}_p, \mathbf{x}_q) + \sigma_n^2 \delta_{pq}$. Here, σ_n^2 is the Gaussian noise and δ_{pq} is the Dirac function. As for the entire training set, we have

$$\mathrm{cov}(\mathbf{y}) = \mathbf{K} + \sigma_n^2 \mathbf{I},$$

where $\mathbf{K} = [k(\mathbf{x}_p, \mathbf{x}_q)] \in \mathbb{R}^{n\times n}$ is the covariance matrix of the training inputs $\mathbf{X}$. The hyperparameters in GPs, denoted by $\Theta = \{\sigma_n^2, \sigma_f^2, l\}$, can be learned from the training data by maximizing the log likelihood of observations.

Given any input $\mathbf{x}_*$, the posterior distribution over function values $f(\mathbf{x}_*)$ is Gaussian,

$$p\left(f(\mathbf{x}_*) \,|\, \mathbf{x}_*, \mathbf{X}, \mathbf{y}\right) = N\left(f(\mathbf{x}_*); \mu_{\mathbf{x}_*}, \sigma_{\mathbf{x}_*}^2\right),$$

where $\mu_{\mathbf{x}_*} = \mathbf{k}_*^{\mathrm{T}}(\mathbf{K} + \sigma_n^2\mathbf{I})^{-1}\mathbf{y}$ and $\sigma_{\mathbf{x}_*}^2 = k(\mathbf{x}_*, \mathbf{x}_*) - \mathbf{k}_*^{\mathrm{T}}(\mathbf{K} + \sigma_n^2\mathbf{I})^{-1}\mathbf{k}_*$. The vector $\mathbf{k}_* \in \mathbb{R}^n$ denotes the covariances between $\mathbf{x}_*$ and the training inputs $\mathbf{X}$. To estimate the corresponding noisy observation y_*, we should consider the noise term ϵ, resulting in the predictive distribution,

$$p\left(y_* \,|\, \mathbf{x}_*, \mathbf{X}, \mathbf{y}\right) = N\left(y_*; \mu_{\mathbf{x}_*}, \sigma_{\mathbf{x}_*}^2 + \sigma_n^2\right). \tag{2}$$

which is a probabilistic regression model of scalar measurements with respect to 2D locations. That is, it can provide the knowledge of uncertainty $\sigma_{\mathbf{x}_*}^2 + \sigma_n^2$ for each expected signal measurement $\mu_{\mathbf{x}_*}$ at any given location $\mathbf{x}_*$. Therefore, GPR can be used to predict new measurements at neighboring locations of the survey trajectory, and accordingly, to create a much denser map representation. The map created by GPR

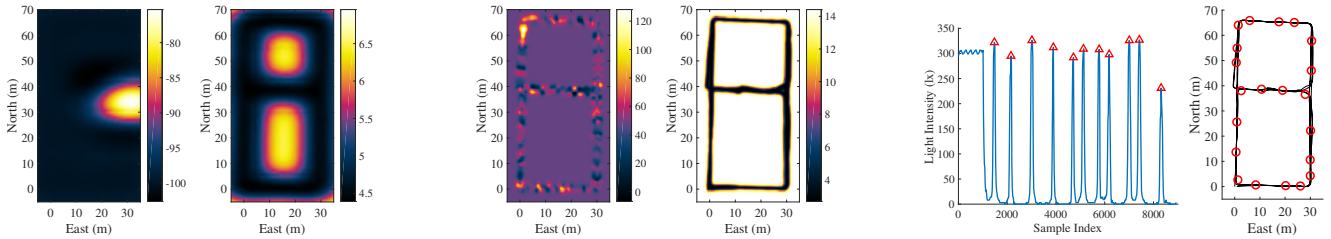

(a) WiFi GPR maps (b) Magnetic GPR maps (c) Lights map

Fig. 7: Example of signal maps. The unit of colorbar is dBm for WiFi maps (a) and μT for magnetic maps (b). The left of (c) shows the peaks with triangle marks on the light intensity signal and the right of (c) shows light locations with circle marks on the optimized trajectory.

is composed of a mean map describing the expected signal measurements and a variance map describing their uncertainties in the surveyed area. The predicted measurements by the GP model have larger variances in places lack of training data (e.g., locations far away from the survey trajectory). Therefore, regions with high variances indicate the unexplored area, while regions with small variances correspond to the traversable area.

By assuming the independence of signal propagation of different WiFi APs, we create GPR maps for each AP separately. As for magnetic fields, we only create the GP model for their magnitudes. Fig. 7 illustrates an example of the generated GPR maps. Especially, we do not use the magnetic field map directly for localization since it is difficult to achieve a comprehensive magnetic map only with the measurements collected along the survey path due to the poor regression properties of magnetic signals [27]. We observe the magnetic variance map approximately matches the corridor layout of the physical floor plan. By contrast, the traversable area indicated by the WiFi variance map is rather expanded due to the large coherence distance of WiFi signals. Considering that the wall-constrained particle filters show great effectiveness in reducing the PDR drift [14], we propose to use the magnetic variance map as a pseudo floor plan for the online localization.

Last but not least, we want to exploit the information of ceiling lights, especially those distributed linearly along narrow corridors, in aid of smartphone localization. The underlying principle will be covered in Section IV-A. In this case, however, we do not expect to obtain a continuous light intensity distribution model with GPR. A major concern arises from the fact that the light intensity readings on the smartphone ambient light sensor can be affected easily by either the user's behavior (e.g., holding the phone at a different pose) or environment dynamics (e.g., temporal blocking by nearby pedestrians). It thus renders the absolute light intensity less predictable in practice. Instead, we resort to a much coarser map representation that contains individual lights, as we can more reliably identify the light spots by detecting peaks of the light intensity signals, as shown in Fig. 7c. As each light spot could be revisited multiple times during the survey, we cluster the detected light spots according to their spatial vicinity to ensure more reliable light detection. Each light is characterized by its central cluster location (i.e., obtained from the optimized walking trajectory associated with timestamps) and a coverage radius (i.e., the light can be detected with a high probability within this coverage). The resulting lights map is then composed of each detected light with a description of its location and coverage vicinity, as shown in Fig. 7c. Note that we can not get to know each light with a unique identity like what happens in visible light communication. All that we have in the lights map is a probabilistic distribution of lights with respect to locations. We will then use it as an observation model in the proposed particle filtering localization.

IV. Localization using Signal Maps

In this section, we present an approach to real-time localization using the generated signal maps by particle filtering.

A. Pseudo Wall and Lights Constraints

Instead of physical floor plans, we employ the GPR variance map of magnetic fields as a pseudo floor plan. This pseudo map provides wall constraints to help with the heading and step length estimation. As illustrated in Fig. 7b, the variance map of the magnetic fields indicates approximately the traversable area. The regions with small and large variances resemble the mapped corridors and unmapped areas, respectively. In addition, the lights along the corridor provide more constraints on the step lengths for the particle filtering and help speed up the convergence of the particle filter.

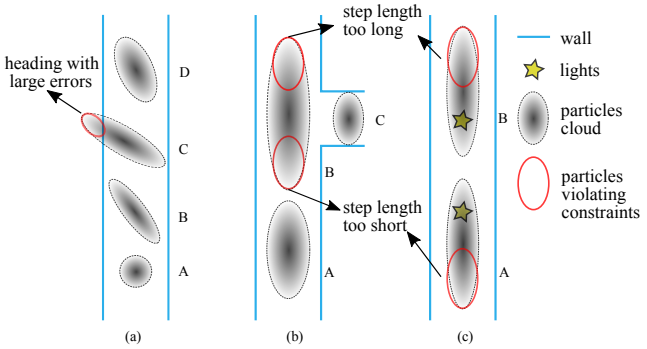

Fig. 8: (a) particles with large heading errors hit the wall and perish while evolving from A to D. (b) particles with either too long or too short step lengths hit the wall when taking a turn. (c) particles violating light constraints get killed at each light detection event.

Fig. 8 demonstrates how the wall constraints and light constraints work on the heading and step length estimation. Intuitively, particles with correct headings will survive after a period of straight walking, while those with large heading errors are more likely to be killed in the importance sampling,

as they violate the wall constraints (see Fig. 8a). The particle cloud is shrunk in the lateral direction but elongated in the walking direction, due to the multi-hypothesis of step lengths. Particles with longer step lengths move faster than those with shorter step lengths. When the user takes a turn, those particles with either too long or too short step lengths will violate the wall constraints and get killed (see Fig. 8b). Upon the detection of light spots (see Fig. 8c), particles beyond the light's coverage vicinity are killed. Similar to the effect of wall constraints during turn-taking, only those particles with moderate step lengths are likely to survive.

B. Particle Filtering

Each particle maintains a hypothesis of the walker's motion state $X = (x, y, \theta, \ell)$, comprising the 2D position (x, y), the heading direction θ, and the step length ℓ. We use a particle cloud $\{X^i\}_{i=1}^{\mathrm{N}}$ along with their importance weights $\{w^i\}_{i=1}^{\mathrm{N}}$ to represent a joint posterior distribution of motion states, where N is number of particles. The particle state is updated at each walking step k using the motion measurements from PDR, namely the step length estimate $\hat{\ell}_k$ and the heading change estimate $\delta\hat{\theta}_k$. Upon the arrival of new observations (e.g., WiFi scans or light spots), the weights for the particle cloud are updated. And if necessary, a new set of particles will be generated from the previous generation through importance re-sampling. The state estimation is achieved by taking the centroid of the existing particle cloud at each step. We follow the general particle filtering procedure with the key steps shown as follows:

Motion Predict: For the ith particle at kth step, the state $\hat{X}_k^i = (x_k^i, y_k^i, \theta_k^i, \ell_k^i)$ is predicted as per

$$\begin{aligned}
\theta_k^i &= \theta_{k-1}^i + \delta\hat{\theta}_k + u_k^i \\
\ell_k^i &= (1-\alpha)\ell_{k-1}^i + \alpha\hat{\ell}_k + v_k^i \\
x_k^i &= x_{k-1}^i - \ell_k^i \sin\theta_{k-1}^i \\
y_k^i &= y_{k-1}^i + \ell_k^i \cos\theta_{k-1}^i,
\end{aligned}$$

where u_k^i and v_k^i are zero-mean Gaussian noises to accommodate the measurement errors in PDR. α is a smoothing factor to account for both the new and historical step lengths.

Observation Update: The overall weights w_k^i are updated by a few separate importance weights that indicate how likely it is that the measurements are consistent with the current particle states. The generic importance weight for the ith particle is $\kappa_i \propto P\left(z_k^i | \hat{X}_k^i\right)$. The weights for the WiFi observation, lights observation, and pseudo wall constraints are written as

$$\kappa_i^{\text{WiFi}} \propto \exp\left\{ \sum_{j=1}^{\mathrm{N}^{\text{WiFi}}} \frac{(\hat{z}_j^{\text{WiFi}} - z_j^{\text{WiFi}})^2}{-2(\hat{\sigma}_j^{\text{WiFi}})^2} \right\}, \tag{3}$$

where $\hat{z}_j^{\text{WiFi}}$ and z_j^{WiFi} are the predicted and real WiFi signal measurements for the jth WiFi AP, respectively, N^{WiFi} is the number of observed APs in common, and $(\hat{\sigma}_j^{\text{WiFi}})^2$ is the predicted variance from the WiFi variance maps;

$$\kappa_i^{\text{light}} \propto \exp\left\{ \frac{\min\limits_{1 \le j \le \mathrm{N}^{\text{light}}} \hat{d}_j^2}{-2\sigma_{\text{light}}^2} \right\}, \tag{4}$$

where $\hat{d}_j$ is the predicted distance of the current particle from the jth light in the lights map, $\mathrm{N}^{\text{light}}$ is the number of lights, and σ_{light}^2 indicates the volume of each light's coverage vicinity;

$$\kappa_i^{\text{wall}} \propto \exp\left\{ \frac{\hat{\sigma}_{\text{magn}}^2}{-2\sigma_{\text{wall}}^2} \right\}, \tag{5}$$

where $\hat{\sigma}_{\text{magn}}^2$ is the predicted magnetic signal variance at the current particle location, and σ_{wall}^2 indicates the penalty on particles that violate the pseudo wall constraints.

These weights are normalized to preserve a valid probability distribution over all the particles. As those missing measurements in each step, the corresponding weights are uniformly assigned. For instance, the lights-based weight update is only triggered each time when a light spot is detected. The total weights are updated according to $w_k^i = w_{k-1}^i \cdot \eta\kappa_i^{\text{WiFi}}\kappa_i^{\text{light}}\kappa_i^{\text{wall}}$, where η is a normalization factor. In our implementation, we choose $\sigma_{\text{light}} = 2\,\mathrm{m}$ and $\sigma_{\text{wall}} = 5\,\mu\mathrm{T}$.

Initialization: To enable the global localization, we use maximum-likelihood-estimation (MLE-) based WiFi-only localization to provide the initial location guess, after which particle filtering is used for position tracking. Even though it is possible to rely on particle filtering without point-mass initialization to achieve global localization, the convergence speed of the filter is not guaranteed, especially when running on a resource-constrained smartphone. To further improve the filter convergence, the noisy magnetic heading is used to narrow down the initial heading guess.

V. Evaluation

We evaluate the proposed survey method in our HKUST academic building as well as in a shopping mall, where we may safely expect rich magnetic anomalies, i.e., those induced by ferromagnetic materials in building structures. The majority of our academic building contains separate rooms and narrow corridors that are partitioned by concrete walls and pillars. The mall is more like a large open space lack of concrete partitions. For example, counters from different sellers are scattered in a common area with wide passages interleaved in between. Therefore, our approach may experience different testing conditions such as opportunistic signal properties and walking path consistency due to the effect of physical settings.

We first present the experimental settings in Section V-A. We then present the site survey results in six testing scenarios in Section V-B and analyze the performance of opportunistic heading measurements, loop-closure detection with WiFi similarity checking and trajectory recovery. In Section V-C, we conduct localization tests in a typical office building scenario to validate the usability of generated signal maps for real-world localization. We discuss the limitations of our method in Section V-D.

A. Experimental Settings

We have implemented our method in an offline batch fashion on a desktop PC (CPU Core i7-7700K @4.20 GHz). The GraphSLAM front-end, signal map generation, and offline localization algorithms are all implemented in MATLAB (R2017a), while the back-end is implemented in C++ by

using the famous g2o library[4]. For data collection in the site survey and offline localization experiments, we use an Android smartphone (Samsung Galaxy S5) installed with a third-party sensor data logging app *GetSensorData*[5]. The smartphone is equipped with an IMU sensor (MPU6500, 100 Hz) which includes a 3-axis accelerometer and a 3-axis gyroscope, a 3-axis magnetic field sensor (AK09911C, 10Hz), an ambient light sensor (TMG399X, 6Hz), and a WiFi scanner (e.g., with an average scan rate of 0.2 Hz). Timestamped sensor readings are logged continuously to the smartphone's local memory during walking. Logging files are then ported to the computer for post-processing. We also implement the localization algorithms by developing a demo app in Java using the official Android Studio IDE[6]. Therefore we can evaluate the real-time localization performance in the real world using the generated signal maps. We use the same Android smartphone in the existing localization evaluation.

We have employed a dedicated surveyor for the site survey test. The surveyor should hold the phone steady in front of him and walk at a normal speed along corridors, by keeping its screen facing up (i.e., a normal gesture for texting) and its length direction approximately aligned with the walking direction. We expect the surveyor to actively revisit some points of interest (POI, e.g., intersections or turns) to form loops on the trajectory. The surveyor should start from a selected POI and finally return back to it to complete each survey session. We encourage the surveyor to walk consistently by following the desired route each time revisiting a POI, say as much as possible. We do not have explicit requirements on the path directions. Yet a general rule we follow during our experiments is that we prefer to walk in a consistent direction, e.g., either keep walking clockwise or counter-clockwise. The surveyor may experience some inconvenience. Nevertheless, we believe that it is rewarding to improve survey performance by constraining the surveyor's behavior.

We have collected five datasets (CYT, AC3-1, AC3-2, AC4-1, and AC4-2) from different floors and regions in the academic building and one more (SOGO) from a public shopping mall. The datasets include walking trajectories lasting from $10\,\mathrm{min}$ to $20\,\mathrm{min}$, and cover areas from $2000\,\mathrm{m}^2$ to $4000\,\mathrm{m}^2$. We have observed a rich amount of magnetic anomalies among all the six datasets. We can easily detect around 15 WiFi APs in each office scenario. Meanwhile, the number of APs heard in SOGO is even higher, i.e., reaching around 50 on average. Therefore, our assumption of a dense WiFi AP deployment as well as rich magnetic anomalies can be satisfied on the six datasets. The office datasets involve some typical office settings, such as interconnected narrow corridors in a rectilinear shape (CYT and AC3-2), extremely long straight corridors (AC4-1), and near-rectangular loops joined by straight or curved corridor segments (AC3-1 and AC4-2). The narrow corridors confine the degree of freedom of people's movements and help generate highly consistent walking paths during the survey. Moreover, the geometry layout, containing concrete walls and pillars, increases the spatial diversity of WiFi signals (see Fig. 5a), due to the radio signal blockage and reflection by walls and other obstacles. These distinctive WiFi signals can enable more reliable loop-closure validation by checking the WiFi signal similarity. The SOGO dataset covers a large open area ($2000\,\mathrm{m}^2$) which is lack of physical partitions. Therefore, as illustrated in Fig. 5b, the WiFi signals are less differentiable than those captured in the office datasets. Worse still, it is quite challenging to obtain a consistent walking path during survey in SOGO, due to the lack of geometry constraints in open areas and unpredictable disturbances from the moving passengers.

To testify the usability of signal maps in real-world localization, we chose a typical office environment CYT among the six surveyed scenarios. We conducted both qualitative and quantitative assessments on the localization performance by using the generated signal maps. In the offline test, we visually compared the localization results with a manually-derived reference path on the floor plan, as well as a visual-inertial odometry trajectory collected by a Google Tango tablet. We held the Samsung smartphone and the Tango tablet, side by side at the same time, and collected the sensor data at a normal walking speed. For the online testing, we used the same Android phone installed with our self-developed app. We selected a number of check-points (e.g., some POIs) from the floor plan on the ground and put markers with an indication of each check-point. The ground truth locations were derived manually from the floor plan by knowing the plot scale. During the online testing, we held the phone in the front and walked passing through these markers. We recorded the real-time localization process with first-view camera videos, which were used to capture the ground markers. Afterwards, we replayed these videos and read the reported locations at the check-points to evaluate the real-time localization accuracy.

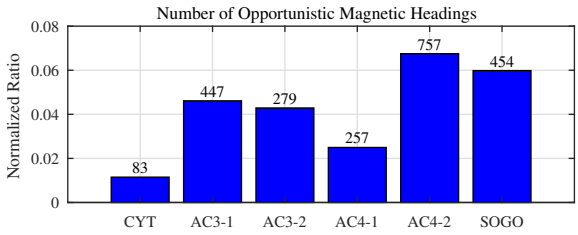

Fig. 9: Number of opportunistic magnetic headings on six datasets.

B. Site Survey Results

1) Opportunistic magnetic headings: We use the number of opportunistic magnetic headings successfully detected on each dataset as a measure of performance. Fig. 9 shows the normalized ratio of the number of detected magnetic headings with respect to the total number of magnetic sensor samples for fair comparison. We did not observe any significant performance loss of our method on the mall dataset (SOGO), compared with other office datasets. In CYT, we can only find 83 heading measurements, i.e., around 1% of the total number of magnetic samples, which are much fewer than those in others. Meanwhile, we have observed salient magnetic distortions in CYT, which are expected to help with loop-closure detection.

[4]https://github.com/RainerKuemmerle/g2o
[5]https://lopsi.weebly.com/downloads.html
[6]https://developer.android.com/studio/

The rationale behind is that we try to opportunistically make use of magnetic observations, i.e., including both magnetic anomalies for loop detection and undistorted magnetic fields for global heading measurements.

2) Loop detection with validation: The statistics on loop-closure correctness are summarized in TABLE I, showing the total number of true positives (TPs) against false positives (FPs) for each dataset using the final optimized trajectories as the ground truth. The pair-wise distances are computed between the optimized poses that are previously designated with loop-closure constraints via magnetic matching. We assume the loop-closure as false positives if the corresponding distance exceeds a given threshold ($5\,\mathrm{m}$ in our implementation). As shown in TABLE I, false positives are significantly rejected by checking the WiFi sequence similarity. The effectiveness of the proposed loop-closure validation method is thus proved. As g2o is sensitive to false positive constraints even with a robust kernel in use, we choose a strict similarity checking threshold that successfully rejects all the false positives. However, a certain portion of true positives are removed as a side effect (see columns for CYT and AC4-1). Note that a less strict threshold is feasible if we use a more robust back-end.

TABLE I: Statistics on TPs/FPs of the detected loop-closures before and after the WiFi signal similarity validation.

Dataset	CYT	AC3-1	AC3-2	AC4-1	AC4-2	SOGO
Before	$\frac{2156}{289}$	$\frac{1038}{873}$	$\frac{322}{215}$	$\frac{1162}{2430}$	$\frac{610}{80}$	$\frac{223}{157}$
After	$\frac{1366}{0}$	$\frac{916}{0}$	$\frac{322}{0}$	$\frac{591}{0}$	$\frac{610}{0}$	$\frac{113}{0}$

3) Trajectory recovery: We evaluate the trajectory recovery performance on the six datasets, as shown in Fig. 10. The four columns from left to right in Fig. 10 show respectively, 1) the raw PDR-derived trajectories before optimization, 2) the optimized trajectories without using opportunistic magnetic heading measurements, 3) the final optimized trajectories with the opportunistic magnetic heading measurements, and 4) the pseudo-ground truth trajectories that are manually labeled on floor plans. Note that the floor plan is used only for visualization in this context.

The raw PDR trajectories reveal the drift-prone nature of odometry especially with low-cost inertial sensors on commercial smartphones. However, some relative motion patterns can be correctly measured, e.g., the long straight walking trace and left/right/U-turns. Note that these motion patterns are also utilized by our method to help with loop-closure detection. We intend to obtain globally consistent and drift-free trajectories by graph optimization, i.e., by exploiting loop-closure constraints and global heading constraints. We are interested in evaluating the contribution of opportunistic magnetic heading measurements to the optimization results. By involving only loop-closure constraints into the GraphSLAM back-end, we are able to get more consistent trajectories compared with raw PDR results. The optimized path in CYT can visually match the reference path. But the results on other datasets are still not globally consistent. After we introduce the opportunistic magnetic heading measurements, the final optimized results turn to be highly consistent and geographically referenced, as shown in Fig. 10. Most of them can match the floor plan reference well by visual inspection. The result for SOGO is not yet satisfying, e.g., some path segments deviate significantly from its reference. We will explain as follows.

As shown in TABLE I, we can find 223 loop-closures with 113 true positives in SOGO (12.6 min). In comparison, we have detected 2156 loop-closures with 1366 true positives in CYT (12.0 min), i.e., bearing a similar survey period. The number of loop-closures is much smaller in SOGO than in other datasets. This is probably due to 1) less consistent survey trajectory and 2) less differentiable WiFi fingerprints. On the one hand, it is quite challenging to obtain a consistent walking path during the survey in SOGO, due to the lack of geometry constraints in open areas and unpredictable disturbances from the moving passengers. On the other hand, WiFi signals are less distinctive in an open space than in a constrained space, due to the lack of spatial diversity, e.g., usually caused by radio signal reflection and blocking by physical partitions. Meanwhile, we have obtained a rich amount of opportunistic magnetic headings in SOGO. They play critical roles in the optimization, especially due to the lack of sufficient loop-closure constraints. Without the help of magnetic heading measurements, our survey method can not even create a globally consistent trajectory in SOGO.

TABLE II: Statistics on the ROE errors of the optimized trajectories.

Dataset	CYT	AC3-1	AC3-2	AC4-1	AC4-2	SOGO
Error (m)	0.87	2.44	2.99	8.10	6.67	22.32

In this evaluation, we are unable to perform a quantitative analysis of the absolute trajectory accuracy due to the lack of tractable ground truths in the testing environments. Alternatively, we characterize "how accurately the surveyor returns to the origin" as a return-to-origin error (ROE), since the surveyor must return to the starting point to complete each survey. The statistics are shown in TABLE II. The results are scaled by a proper factor that is experimentally decided to accommodate the scale ambiguity. The ROE error for CYT ($0.87\,\mathrm{m}$) is considerably small. We credit this good performance to both the rich magnetic anomalies induced by the building construction materials and the narrow corridors that strictly confine the survey path. The ROE errors for other office areas range from $2.44\,\mathrm{m}$ to $8.10\,\mathrm{m}$. We attribute the different performance to various magnetic signal distributions and WiFi signal properties under different physical settings of the testing environments, as well as varying coverage areas. The extremely large ROE error in SOGO ($22.32\,\mathrm{m}$) shows the worse performance of our survey method in an open area than in space-constrained environments.

C. Localization Results

In this section, we conduct both qualitative and quantitative assessments on the localization using the generated signal maps for CYT. We use 1000 particles throughout this experiment. The reference trajectory originates from the left-bottom corner, travels along the corridor segments clockwisely, closes two loops and finally returns to the origin.

	Raw PDR path	SLAM path w/o mag. heading	SLAM path w/ mag. heading	Reference path on floor plan
CYT (12.0 min)	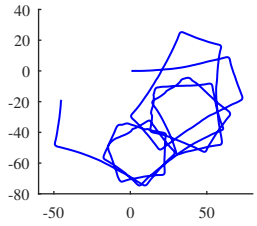 (a)	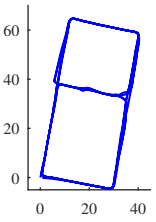 (b)	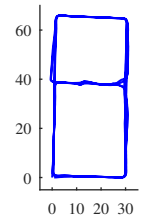 (c)	 (d)
AC3-1 (16.1 min)	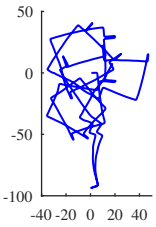 (e)	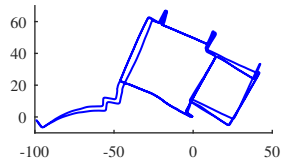 (f)	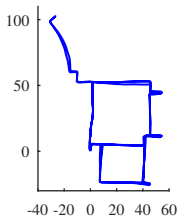 (g)	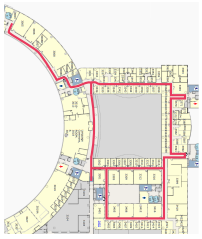 (h)
AC3-2 (10.8 min)	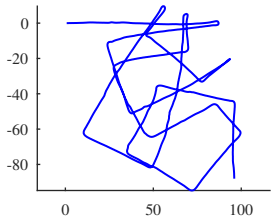 (i)	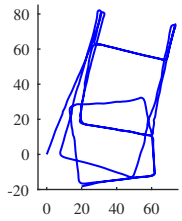 (j)	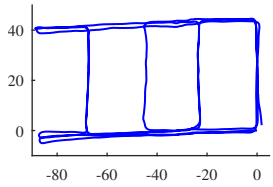 (k)	 (l)
AC4-1 (17.1 min)	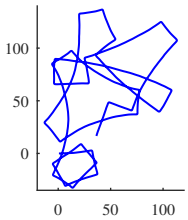 (m)	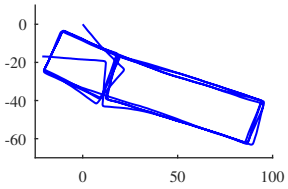 (n)	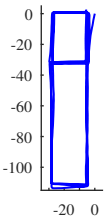 (o)	 (p)
AC4-2 (18.7 min)	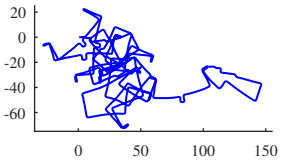 (q)	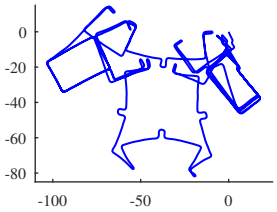 (r)	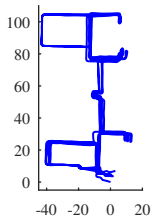 (s)	 (t)
SOGO (12.6 min)	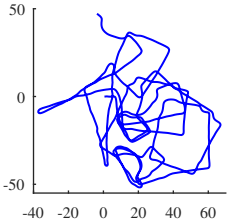 (u)	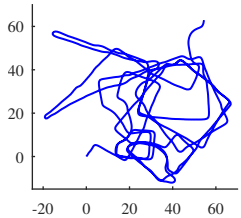 (v)	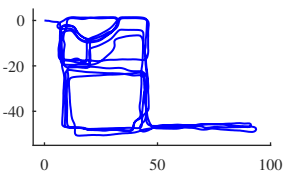 (w)	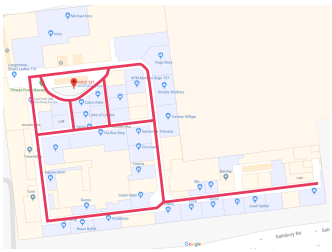 (x)

Fig. 10: Trajectory recovery results in six survey scenarios (CYT, AC3-1, AC3-2, AC4-1, AC4-2, and SOGO). The x-axis and y-axis are the 2D position coordinates measured in meters. In specific, the x-axis and y-axis of figures in column "SLAM path w/ mag. heading" are aligned with the geomagnetic East and North, respectively.

We tested three localization algorithms, namely MLE-based WiFi-only localization and the proposed particle filtering-based localization using the generated signal maps both with and without light measurements.

1) Running offline: Fig. 11 shows the offline localization results with light measurements enabled in (a) and disabled in (b). The filtered trajectory with light observations show high consistency with the corridor layout. The WiFi-only localization results are scattered across the test area, e.g., due to the lack of motion constraints and structural constraints. The visual-inertial odometry trajectory obtained by Tango is shown against the floor plan for visual comparison. We observe clear drifts in Tango's path, as highlighted by the dash-dot rectangle in Fig. 11a. By contrast, the results of the proposed method are constrained well in the corridor region. Without involving the observations of lights, the estimated trajectory deviates severely from the corridor at some locations, as shown in 11b. The performance degradation is due to the lack of constraints on step lengths when walking along the straight corridor. Yet the walking direction is still well-estimated thanks to the pseudo wall constraints.

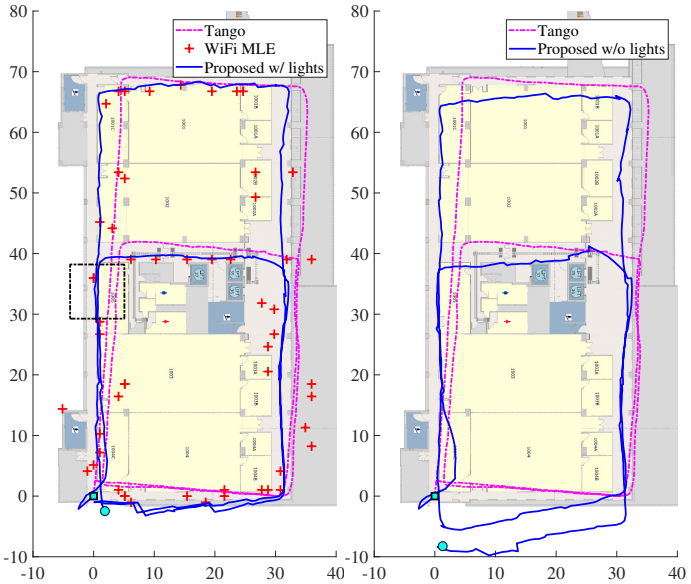

(a) Light measurements enabled (b) Light measurements disabled

Fig. 11: Offline localization results. The x-axis and y-axis are the 2D position coordinates measured in meters. The square indicates the start and the circle indicates the end of the estimated trajectories.

2) Running online: We developed an Android app, as shown in Fig. 12a, to evaluate the real-time localization performance on the smartphone. The testing trajectory is the same one as in the last section. We have computed the pair-wise Euclidean errors at 40 check-points with known locations and plotted the empirical cumulative distribution (CDF) of location estimation errors in Fig. 12b. Statistics on the localization accuracy are summarized in TABLE III.

The 90th percentile accuracy of MLE-based WiFi-only localization is $9.52\,\mathrm{m}$ (see *MLE*), which is reasonable for the performance of WiFi fingerprinting-based localization. The 90th percentile accuracy of the proposed method without light measurements is $5.97\,\mathrm{m}$ (see *PF-w/o*), which is significantly better than the WiFi-only localization. This is because we have involved the motion measurements from PDR and pseudo-wall constraints to help confine the walking path. We also observe large errors (e.g., $32\,\mathrm{m}$) for the proposed method with light measurements disabled. We attribute the large errors to the initialization stage of particle filtering. The location estimation accuracy can improve with time as the particle filter converges.

TABLE III: Statistics on the localization accuracy (online).

Algo.	MLE	PF-w/o	PF-w/ (1st)	PF-w/ (2nd)
50-ile Error (m)	5.35	3.04	2.45	2.30
90-ile Error (m)	9.52	5.97	5.46	3.41

We take two consecutive trials for the proposed method with light measurements enabled (see *PF-w/(1st)* and *PF-w/(2nd)*). That is, we keep walking at the end of the first round, circumventing the initialization process of particle filtering for the second round evaluation. In the first round, the 90th percentile accuracy is $5.46\,\mathrm{m}$, which is even better than that with light measurements disabled. This is credited to the lights map which provides additional constraints on step lengths. In the second round, the 90th percentile accuracy is $3.41\,\mathrm{m}$, which is further improved as expected.

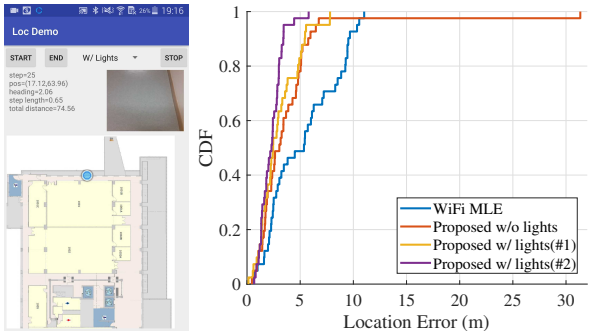

(a) Demo app (b) Location error CDF

Fig. 12: Localization results in online testing. The blue dot in (a) indicates the estimated location in real-time.

D. Discussions

The performance of our method could be affected by several practical issues which will be covered in the following.

Opportunistic observations. In spite of the ubiquitous existence of magnetic fields, magnetic anomalies and undisturbed magnetic headings are indeed opportunistic observations. The occurrence of magnetic anomalies is mainly affected by building structures and working electronic devices. We rely on these anomalies for reliable magnetic sequence matching and loop-closure detection. Meanwhile, opportunistic magnetic headings are also exploited for the graph optimization. Therefore, the survey performance is subject to the operating environments. Regardless, we think it is reasonable as we only use free ambient signals in this work.

Space-constrained office buildings. During our experiments, we observe that our approach performs better in space-constrained office buildings than in an open-spaced shopping

mall. The most probable reasons are two-fold: 1) a narrow space has more constraints on the surveyor's movement freedom and help improve the survey path consistency, and 2) WiFi fingerprints are more distinctive in an office environment with complex layouts due to the blockage and refection of radio signals. In addition, we also find that steel materials in building structures will induce more significant magnetic distortions in their neighborhood. So we have a better chance to find salient magnetic anomalies in a space-constrained area.

Lights vs. sunlight. We employ the ceiling lights to help constrain the step lengths with a particle filter for localization. The lights are simply detected by peak detection with the smartphone's inbuilt ambient light sensors. The light detection method is not immune to sunlight. For instance, false positives may appear when the user simply rotates his phone in places with direct sunlight exposure. This problem could be solved by examining the frequency spectrum of light signals. Light emitted by fluorescent lights is characterized by some high-order harmonics of strong magnitudes.

Device and user diversity. We only evaluated the localization performance by one user and with a single device, the usability of signal maps on other devices and for other users, have not been proved. The effects of device diversity and user diversity are very important issues to solve, especially for the wide adoption of fingerprinting-based localization. We will leave this problem in our future work. For example, the sensor characteristics and qualities vary significantly across different types of Android devices. We are going to account for the effect of heterogeneous sensors on signal measurements, e.g., by online sensor calibration.

VI. Conclusions

In this paper, we proposed a site survey approach that can automatically build maps of opportunistic signals for indoor localization by a dedicated surveyor using a smartphone. Without any detailed knowledge of the building floor plan, we assume rich magnetic anomalies and dense WiFi AP deployment in a space-constrained environment (e.g., modern office buildings). Under these assumptions, our approach can recover the surveyor's walking trajectory with global consistency and then generate a set of probabilistic maps for opportunistic signals, which can be exploited for online localization within a Bayesian filtering framework.

The site survey approach followed the classical Graph-SLAM framework. To be specific, the front-end constructed a pose graph by incorporating the PDR-derived motion constraints, the loop-closure constraints via magnetic matching, and the global heading constraints from the opportunistic magnetic heading measurements. The back-end generated a globally consistent trajectory via graph optimization for signal map generation. The proposed loop-closure validation method using WiFi signal similarity showed great effectiveness in reducing false positives. The incorporation of opportunistic magnetic heading measurements improved the spatial consistency of our optimization results. We evaluated the proposed site survey approach in both space-constrained office buildings and an open-spaced shopping mall. We achieved globally consistent trajectories in the office scenarios. But the performance in the mall is degraded. We have identified two main reasons, i.e., less consistent walking trajectories of the surveyor and less differentiable WiFi signal properties.

To prove the usability of signal maps in real applications, we evaluated the localization performance by particle filtering in a typical rectilinear office environment. The pseudo wall constraints and the lights constraints worked well in confining the particle cloud. In addition, we demonstrated the real-time localization on a smartphone. The 50th percentile accuracy and 90th percentile accuracy are $2.30\,\mathrm{m}$ and $3.41\,\mathrm{m}$, respectively. Since we only evaluate the localization performance by one person and with the same device, the usability of signal maps on other devices and for other users, have not been testified. We believe that these problems are very important for our research, especially for the real-world adoption of smartphone localization using opportunistic signals. Therefore, we will leave them in our future work.

References

[1] P. Davidson and R. Piché, "A survey of selected indoor positioning methods for smartphones," *IEEE Commun. Surveys Tuts.*, vol. 19, no. 2, pp. 1347–1370, 2017.

[2] K. Liu, X. Liu, and X. Li, "Guoguo: Enabling fine-grained indoor localization via smartphone," in *Proc. A MobiSys*. ACM, 2013, pp. 235–248.

[3] A. Jovicic, "Qualcomm® Lumicast: A high accuracy indoor positioning system based on visible light communication," 2016.

[4] Y. Shu, C. Bo, G. Shen, C. Zhao, L. Li, and F. Zhao, "Magicol: Indoor localization using pervasive magnetic field and opportunistic WiFi sensing," *IEEE J. Sel. Areas Commun.*, vol. 33, no. 7, pp. 1443–1457, 2015.

[5] Y. Sun, M. Liu, and M. Q.-H. Meng, "WiFi signal strength-based robot indoor localization," in *Proc. IEEE International Conference on Information and Automation (ICIA)*. IEEE, 2014, pp. 250–256.

[6] Q. Xu, R. Zheng, and S. Hranilovic, "IDyLL: indoor localization using inertial and light sensors on smartphones," in *Proc. UbiComp*. ACM, 2015, pp. 307–318.

[7] Q. Liang, L. Wang, Y. Li, and M. Liu, "Plugo: a Scalable Visible Light Communication System towards Low-cost Indoor Localization," in *Proc. IROS*. IEEE, 2018, pp. 3709–3714.

[8] H. Liu, H. Darabi, P. Banerjee, and J. Liu, "Survey of wireless indoor positioning techniques and systems," *IEEE Trans. Syst. Man Cybern. Part C Appl. Rev.*, vol. 37, no. 6, pp. 1067–1080, 2007.

[9] K. Lin, M. Chen, J. Deng, M. M. Hassan, and G. Fortino, "Enhanced fingerprinting and trajectory prediction for IoT localization in smart buildings," *IEEE Trans. Autom. Sci. Eng.*, vol. 13, no. 3, pp. 1294–1307, 2016.

[10] H. Xie, T. Gu, X. Tao, H. Ye, and J. Lu, "A reliability-augmented particle filter for magnetic fingerprinting based indoor localization on smartphone," *IEEE Trans. Mobile Comput.*, vol. 15, no. 8, pp. 1877–1892, 2016.

[11] C. Gao and R. K. Harle, "Semi-automated signal surveying using smartphones and floorplans," *IEEE Trans. Mobile Comput.*, 2017.

[12] S. Wang, H. Wen, R. Clark, and N. Trigoni, "Keyframe based large-scale indoor localisation using geomagnetic field and motion pattern," in *Proc. IROS*, 2016, pp. 1910–1917.

[13] C. E. Rasmussen, "Gaussian processes for machine learning," 2006.

[14] A. Rai, K. K. Chintalapudi, V. N. Padmanabhan, and R. Sen, "Zee: Zero-effort crowdsourcing for indoor localization," in *Proc. Mobicom*. ACM, 2012, pp. 293–304.

[15] H. Wang, S. Sen, A. Elgohary, M. Farid, M. Youssef, and R. R. Choudhury, "No need to war-drive: Unsupervised indoor localization," in *Proc. MobiSys*. ACM, 2012, pp. 197–210.

[16] C. Wu, Z. Yang, and Y. Liu, "Smartphones based crowdsourcing for indoor localization," *IEEE Trans. Mobile Comput.*, vol. 14, no. 2, pp. 444–457, 2015.

[17] H. Shin, Y. Chon, and H. Cha, "Unsupervised construction of an indoor floor plan using a smartphone," *IEEE Trans. Syst. Man Cybern. Part C Appl. Rev.*, vol. 42, no. 6, pp. 889–898, 2012.

[18] Y. Kim, Y. Chon, and H. Cha, "Smartphone-based collaborative and autonomous radio fingerprinting," *IEEE Trans. Syst. Man Cybern. Part C Appl. Rev.*, vol. 42, no. 1, pp. 112–122, 2012.

[19] Z. Peng, S. Gao, B. Xiao, S. Guo, and Y. Yang, "CrowdGIS: Updating digital maps via mobile crowdsensing," *IEEE Trans. Autom. Sci. Eng.*, vol. 15, no. 1, pp. 369–380, 2018.

[20] J. Huang, D. Millman, M. Quigley, D. Stavens, S. Thrun, and A. Aggarwal, "Efficient, generalized indoor WiFi graphSLAM," in *Proc. ICRA*. IEEE, 2011, pp. 1038–1043.

[21] R. Faragher, C. Sarno, and M. Newman, "Opportunistic radio SLAM for indoor navigation using smartphone sensors," in *Proc. IEEE/ION Position Location and Navigation Symposium (PLANS)*. IEEE, 2012, pp. 120–128.

[22] R. M. Faragher and R. K. Harle, "Towards an efficient, intelligent, opportunistic smartphone indoor positioning system," *Navigation*, vol. 62, no. 1, pp. 55–72, 2015.

[23] T. D. Barfoot, *State Estimation for Robotics*. Cambridge University Press, 2017.

[24] Y. Sun, M. Liu, and M. Q.-H. Meng, "Motion removal for reliable RGB-D SLAM in dynamic environments," *Robotics and Autonomous Systems*, vol. 108, pp. 115–128, 2018.

[25] ——, "Improving RGB-D SLAM in dynamic environments: A motion removal approach," *Robotics and Autonomous Systems*, vol. 89, pp. 110–122, 2017.

[26] R. Harle, "A survey of indoor inertial positioning systems for pedestrians," *IEEE Commun. Surveys Tuts.*, vol. 15, no. 3, pp. 1281–1293, 2013.

[27] C. Gao and R. Harle, "Sequence-based magnetic loop closures for automated signal surveying," in *Proc. IPIN*. IEEE, 2015, pp. 1–12.

[28] H. Ren and P. Kazanzides, "Investigation of attitude tracking using an integrated inertial and magnetic navigation system for hand-held surgical instruments," *IEEE/ASME Trans. Mechatronics*, vol. 17, no. 2, pp. 210–217, 2012.

[29] G. Grisetti, R. Kummerle, C. Stachniss, and W. Burgard, "A tutorial on graph-based SLAM," *IEEE Intell. Transp. Syst. Mag.*, vol. 2, no. 4, pp. 31–43, 2010.

[30] C. Zhang and X. Zhang, "LiTell: indoor localization using unmodified light fixtures," in *Proc. MobiCom*. ACM, 2016, pp. 481–482.

[31] G. Shen, Z. Chen, P. Zhang, T. Moscibroda, and Y. Zhang, "Walkie-markie: Indoor pathway mapping made easy," in *Proc. NSDI*. USENIX Association, 2013, pp. 85–98.

[32] R. Gao, M. Zhao, T. Ye, F. Ye, Y. Wang, K. Bian, T. Wang, and X. Li, "Jigsaw: Indoor floor plan reconstruction via mobile crowdsensing," in *Proc. MobiCom*. ACM, 2014, pp. 249–260.

[33] H. Weinberg, "Using the adxl202 in pedometer and personal navigation applications," *Analog Devices AN-602 application note*, vol. 2, no. 2, pp. 1–6, 2002.

[34] R. Kümmerle, G. Grisetti, H. Strasdat, K. Konolige, and W. Burgard, "g2o: A general framework for graph optimization," in *Proc. ICRA*. IEEE, 2011, pp. 3607–3613.

Qing Liang received the B.A. degree in Automation at Xi'an Jiaotong University (XJTU), Xi'an, China, in 2013 and the master degree in Instrument Science and Technology at Beihang University (BUAA), Beijing, China, in 2016. He is now a PhD student at the Department of ECE, HKUST. His current research interests include sensor fusion, low-cost localization, and mobile robots.

Ming Liu received the B.A. degree in Automation at Tongji University in 2005. During his master study at Tongji University, he stayed one year in Erlangen-Nünberg University and Fraunhofer Institute IISB, Germany, as a master visiting scholar. He graduated as a PhD student from the Department of Mechanical and Process Engineering of ETH Zürich in 2013.

He is now affiliated with ECE department, CSE department and Robotics Institute of Hong Kong University of Science and Technology. His research interests include dynamic environment modeling, deep-learning for robotics, 3D mapping, machine learning and visual control.

Prof. Liu is the recipient of the Best Student Paper Award at IEEE MFI 2012, the Best Paper in Information Award at IEEE ICIA 2013, the Best RoboCup Paper at IEEE IROS 2013, and twice the Winning Prize of the Chunhui-Cup Innovation Contest.